





# Competing gauge fields and entropically driven spin liquid to spin liquid transition in non-Kramers pyrochlores

Daniel Lozano-Gómez<sup>a,b,1</sup>, Vincent Noculak<sup>c,d</sup>, Jaan Oitmaa<sup>e</sup>, Rajiv R. P. Singh<sup>f</sup>, Yasir Iqbal<sup>g</sup> , Johannes Reuther<sup>c,d,g</sup>, and Michel J. P. Gingras<sup>a</sup> 

Affiliations are included on p. 9.

Edited by J. C. Davis, University of Oxford, Oxford, United Kingdom; received February 20, 2024; accepted June 10, 2024

Gauge theories are powerful theoretical physics tools that allow complex phenomena to be reduced to simple principles and are used in both high-energy and condensed matter physics. In the latter context, gauge theories are becoming increasingly popular for capturing the intricate spin correlations in spin liquids, exotic states of matter in which the dynamics of quantum spins never ceases, even at absolute zero temperature. We consider a spin system on a three-dimensional pyrochlore lattice where emergent gauge fields not only describe the spin liquid behavior at zero temperature but crucially determine the system's temperature evolution, with distinct gauge fields giving rise to different spin liquid phases in separate temperature regimes. Focusing first on classical spins, in an intermediate temperature regime, the system shows an unusual coexistence of emergent vector and tensor gauge fields where the former is known from classical spin ice systems while the latter has been associated with fractonic quasiparticles, a peculiar type of excitation with restricted mobility. Upon cooling, the system transitions into a low-temperature phase where an entropic selection mechanism depopulates the degrees of freedom associated with the tensor gauge field, rendering the system spin-ice-like. We further provide numerical evidence that in the corresponding quantum model, a spin liquid with coexisting vector and tensor gauge fields has a finite window of stability in the parameter space of spin interactions down to zero temperature. Finally, we discuss the relevance of our findings for non-Kramers magnetic pyrochlore materials.

spin liquids | entropic selection | liquid-to-liquid crossover | competing gauge fields | frustrated magnetism

Gauge symmetries and their embodiment within pertinent mathematical frameworks constitute a quintessential aspect of some of the most fundamental theories of physics, ranging from Maxwell's electromagnetism and Einstein's general relativity to the standard model of particle physics. In such fundamental theories, different types of gauge fields usually coexist but are of physical relevance only within a characteristic energy scale. Over the past 40 years or so, the application of gauge theories in condensed matter physics to describe strongly correlated electron and magnetic (spin) systems has steadily grown (1–3). In the contemporary field of highly frustrated magnetism (4, 5), gauge symmetries can emerge from the energetic constraints on the allowed spin orientations that are imposed by competing (i.e., frustrated) spin–spin interactions. The latter can significantly enhance the magnitude of thermal and quantum fluctuations, thus undermining the development of conventional long-range magnetic order, but still stabilizing strong nontrivial spatiotemporal correlations between the spins, producing a liquid-like state of sorts—a spin liquid (4–9).

Gauge theories have proven powerful schemes to describe a wide range of spin liquids (10–13). In particular, the usage of such theories has allowed to uncover various spin liquid states harbored by magnetic systems whose spins reside on the vertices of the three-dimensional pyrochlore lattice of corner-sharing tetrahedra and to expose their exotic properties (14–17). For example, the spin liquid state found at low temperatures in spin ice materials (15) [e.g.,  $R_2M_2O_7$  ( $R = \text{Ho, Dy}$ ;  $M = \text{Ti, Sn, Ge}$ ) (18)] is characterized by constrained orientations of the magnetic moments that are akin to an effective Gauss' law describable by an emergent gauge field (14, 15). This elegant description has direct experimental consequences, namely, the spin–spin correlations show nonanalytical “pinch point” singularities in reciprocal (momentum) space that are revealed in neutron scattering experiments (19, 20), thus bearing witness to the underlying gauge symmetry describing the spin ice state (21, 22).

Classical spin liquids (CSLs) have extensive ground state degeneracy arising from fine-tuned sets of spin–spin interactions (11, 23, 24) and are potential harbingers of quantum spin liquids (QSLs) upon consideration of the spins' quantum dynamics

## Significance

Competing interactions in magnetic systems frustrate the development of long-range order, possibly down to absolute zero temperature, giving rise to a spin liquid. Gauge fields, akin to those used to describe the fundamental forces in the universe, are the mathematical objects of choice to describe spin liquids. In a model relevant to real magnetic pyrochlore materials, we uncover a spin liquid described by combined vector-like and matrix-like gauge fields. Classically, similarly to the liquid-to-liquid transition observed in some molecular liquids, this state disappears at low temperatures and gives way to a spin liquid with extensive entropy and with only the vector-like field thermally fluctuating. Quantum mechanically, the ground state is a spin liquid described by both gauge fields.

Author contributions: Y.I., J.R., and M.J.P.G. designed research; D.L.-G., V.N., J.O., and R.R.P.S. performed research; D.L.-G., V.N., J.O., R.R.P.S., J.R., and M.J.P.G. analyzed data; and D.L.-G., V.N., R.R.P.S., Y.I., J.R., and M.J.P.G. wrote the paper.

The authors declare no competing interest.

This article is a PNAS Direct Submission.

Copyright © 2024 the Author(s). Published by PNAS. This article is distributed under [Creative Commons Attribution-NonCommercial-NoDerivatives License 4.0 \(CC BY-NC-ND\)](https://creativecommons.org/licenses/by-nc-nd/4.0/).

<sup>1</sup>To whom correspondence may be addressed. Email: daniel.lozano-gomez@tu-dresden.de.

This article contains supporting information online at <https://www.pnas.org/lookup/suppl/doi:10.1073/pnas.2403487121/-DCSupplemental>.

Published August 28, 2024.

(25–27). However, in the classical limit, ground state degeneracies are generically lifted by arbitrary small (perturbative) symmetry-allowed interactions thence typically inducing long-range magnetic order. One can flip this perspective around to anticipate that CSLs, and thus QSLs, ought to often manifest themselves at the phase boundary between magnetically ordered classical ground states, as noted in prominent examples (12, 28). Within this line of thought, and inspired by the successes of the gauge theory description of spin ice (14, 15), a number of works on pyrochlore spin systems have shown that diverse gauge symmetries can arise at the boundary of competing classical long-range ordered phases, signaling new types of CSLs (16, 17) and thus, potentially novel QSLs. Examples include reports of a “pinch-line spin liquid” (17) and a rank-2 U(1) spin liquid (16), both of which described by emergent tensorial gauge fields. The latter spin liquid is of particular interest because it is described by a symmetric rank-2 tensor gauge field akin to that present in theories of fractons, spin excitations that can only propagate on subdimensional spaces (29).

The aforementioned successes beg the question “what new spin-liquid physics, at the classical or quantum level, may be evinced when three classical phases meet at a triple point?” This is the question we investigate in this paper by considering an effective spin-1/2 model for pyrochlore magnets of interacting non-Kramers rare-earth ions (i.e., that possess an even number of electrons) (30–32) in a region of spin–spin couplings parameter space where three phases meet: one magnetic dipolar (spin ice) spin liquid phase and two electric quadrupolar long-range ordered phases (30–32). We refer to this magnetic triple point as a dipolar–quadrupolar–quadrupolar (DQQ) point. We find that the gauge symmetries at that point are enlarged due to competing and energetically degenerate rank-1 ( $R_1$ ) and rank-2 ( $R_2$ ) gauge fields, resulting in a spin liquid that we refer to as a  $R_1$ - $R_2$  spin liquid. Most interestingly, we find that upon cooling, the rank-2 gauge field freezes out while the rank-1 U(1) spin ice liquid gets progressively entropically selected below a crossover temperature  $T^*$ . We thus observe a phenomenon of spin liquid to spin liquid rapid thermal crossover in a magnetic system that is solely driven by temperature for a fixed spin Hamiltonian and not by tuning a parameter of the Hamiltonian as happens in the models considered in refs. 33 and 34. Here, we refer to “spin liquid” as a cooperative paramagnetic phase (35) that does not spontaneously break any of the symmetries of the Hamiltonian. Such thermodynamic behavior reminds one of the liquid-to-liquid transition observed in some atomic and molecular liquids (36, 37). We note that recent work (38) found a temperature-driven transition separating two phases lacking long-range magnetic (i.e., dipolar) order. However, in contrast with ref. 38 wherein the two phases considered are a spin liquid phase and a symmetry-broken nematic phase, in the model under investigation in the present work, both phases preserve all symmetries of the parent Hamiltonian down to zero temperature.

Incorporating the effects of quantum spin fluctuations in our model, we find a window of spin–spin couplings close to the triple point where the system fails to display long-range magnetic order, thus providing evidence for a putative QSL. These results are not only interesting from a strictly theoretical point of view but may be of relevance for understanding the highly paradoxical non-Kramers  $\text{Tb}_2\text{M}_2\text{O}_7$  ( $M = \text{Ti, Sn, Ge}$ ) pyrochlore magnets (7, 32). This may be particularly so for  $\text{Tb}_2\text{Ti}_2\text{O}_7$ , which has defied understanding since it was first studied (39) and for which recent work (40) proposed that this material may actually reside in the vicinity of such a DQQ triple point.

## Results

**Model, Irrep Analysis, and Monte Carlo Results.** The nearest-neighbor spin Hamiltonian,  $\mathcal{H}$ , for a non-Kramers system is described in terms of three spin–spin coupling constants  $\{J_{zz}, J_{\pm}, J_{\pm\pm}\}$ , with  $\mathcal{H}$  given by

$$\mathcal{H} = \sum_{\langle ij \rangle} J_{zz} S_i^z S_j^z - J_{\pm} (S_i^+ S_j^- + S_i^- S_j^+) + J_{\pm\pm} (\gamma_{ij} S_i^+ S_j^+ + \gamma_{ij}^* S_i^- S_j^-), \quad [1]$$

where  $S_i^\alpha$  is the  $\alpha$ th component of the (pseudo) spin-1/2 on site  $i$  in a local coordinate frame (*SI Appendix*), with  $S_i^z$  representing magnetic dipolar degrees of freedom and  $S_i^\pm$  representing electric quadrupolar degrees of freedom (31, 32).  $\langle ij \rangle$  labels the nearest-neighbor pyrochlore bonds between sites  $i$  and  $j$  and  $\gamma_{ij}$  are phase factors imposed by the lattice symmetry (31, 32). We take  $J_{zz} > 0$  to stabilize a spin ice state when  $J_{\pm} = J_{\pm\pm} = 0$ . To identify the classical ordered phases of  $\mathcal{H}$ , we first decompose it in terms of the irreducible representations (irreps) of a tetrahedron (41, 42, and *SI Appendix*). We write

$$\mathcal{H} = \sum_{\boxtimes} \mathcal{H}^{\boxtimes} = \sum_{\boxtimes} \sum_{i,j \in \boxtimes} \mathbf{S}_i^T \mathbf{M}_{ij} \mathbf{S}_j, \quad [2]$$

where  $\mathcal{H}^{\boxtimes}$  is the single-tetrahedron Hamiltonian,

$$\mathcal{H}^{\boxtimes} = \frac{1}{2} \left[ a_{T_1^{\text{lcc}}} \left( \mathbf{m}_{T_1^{\text{lcc}}}^{\boxtimes} \right)^2 + a_E \left( \mathbf{m}_E^{\boxtimes} \right)^2 + a_{T_1^{\text{xy}}} \left( \mathbf{m}_{T_1^{\text{xy}}}^{\boxtimes} \right)^2 + a_{A_2} \left( \mathbf{m}_{A_2}^{\boxtimes} \right)^2 + a_{T_2} \left( \mathbf{m}_{T_2}^{\boxtimes} \right)^2 \right]. \quad [3]$$

Here,  $\{\mathbf{m}_I^{\boxtimes}\}$  are the single-tetrahedron irrep spin modes which diagonalize  $\mathcal{H}^{\boxtimes}$ . The  $a_I$  parameters are linear functions of the couplings  $\{J_{zz}, J_{\pm}, J_{\pm\pm}\}$  and correspond to the energies associated with irrep  $I$  (see *SI Appendix*). In this representation, the  $T_1^{\text{xy}}$  and the  $T_1^{\text{lcc}}$  irreps correspond to two splayed ferromagnetic spin configurations, whereas the remaining  $A_2$ ,  $E$ , and  $T_2$  irreps correspond to different antiferromagnetic spin configurations (41). We refer the reader to the *SI Appendix* for further details regarding the determination of the  $a_I$  parameters and the spin configuration associated with each irrep  $I$ .

From Eq. 3, the classical ground state phase diagram follows immediately and is shown in Fig. 1A (31, 40, 43). There are four triple points in the phase diagram: Three of these correspond to the corners of the gray  $T_1^{\text{lcc}}$  triangle and one to the intersection of the  $T_1^{\text{lcc}}$ , the  $E(\psi_2)$ , and the  $E(\psi_3)$  phases. At that point, thermal fluctuations stabilize the  $E$  phase which partially invades over the  $T_1^{\text{lcc}}$ , with a transition from paramagnetic to long-range order in the  $E$  phase order upon decreasing temperature (43). We also note that, for the quantum spin-1/2 case, this triple point is near the phase boundary (on the  $J_{\pm\pm} = 0$  axis where there is a Higgs transition between a quantum spin ice phase and a U(1) magnetic long-range ordered phases (44). We do not investigate this  $T_1^{\text{lcc}}-E(\psi_2)-E(\psi_3)$  triple point further in the present work. The leftmost triple point (black circle) corresponds to the local Heisenberg antiferromagnet (HAF) model (43), dual to the highly studied global HAF model (32), the latter model known to realize a Coulomb phase spin liquid (45–48).

The lower triple point (white circle) is located on the phase boundary between the  $E$ , the  $T_1^{\text{xy}}$ , and the  $T_1^{\text{lcc}}$  phases. This is the

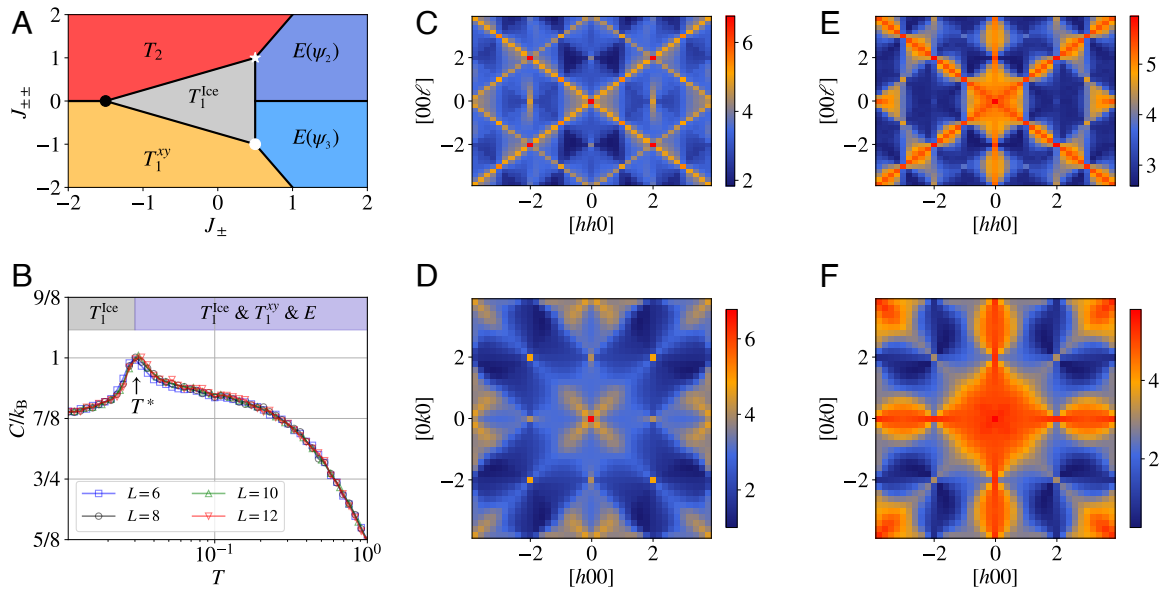


**Fig. 1.** (A) Non-Kramers phase diagram with  $J_{zz} = 3$ , where the DQQ model corresponds to the white dot at the boundary between the classical  $T_1^{xy}$ ,  $E(\psi_3)$ , and  $T_1^{lce}$  phases. (B) Specific heat of the DQQ model obtained from Monte Carlo simulations for various system sizes where a bump at a temperature  $T^* \sim 0.03$  in the specific heat that signals a crossover between an intermediate-temperature and a low-temperature regime, further discussed in the main text, is observed. This crossover is characterized by an entropically driven depopulation of the  $E$  and  $T_1^{xy}$  irrep modes, as discussed and illustrated in model details in Fig. 1. Spin structure factors in the  $[hh\ell]$  (C) and  $[hk0]$  (D) planes for a temperature just above the crossover temperature  $T^*$ . Spin structure factors in the  $[h\ell\ell]$  (E) and  $[hk0]$  (F) planes for a temperature below the crossover temperature  $T^*$ .

DQQ point alluded in the introduction, with the finely-tuned parameters  $\{J_{zz} = 3, J_{\pm\pm} = \frac{1}{2}, J_{\pm\pm\pm} = -1\}$  defining what we refer to as the DQQ model, and which constitutes the primary focus of the present study. The exchange couplings at this specific point can also be parameterized by a global ferromagnetic Heisenberg coupling and the so-called indirect Dzyaloshinskii–Moriya (DM) interaction (49), namely

$$\mathcal{H} = -J \sum_{\langle ij \rangle} \mathbf{S}_i \cdot \mathbf{S}_j + D \sum_{\langle ij \rangle} \mathbf{d}_{ij} \cdot (\mathbf{S}_i \times \mathbf{S}_j), \quad [4]$$

where  $\mathbf{d}_{ij}$  are the DM vectors as defined in ref. 42 and the interaction parameters satisfy  $D/J = -2$ . For more details on the  $\mathbf{d}_{ij}$  vectors and the sign convention, we refer the reader to the *SI Appendix*. Previous work (42) noted an apparent lack of magnetic ordering at this triple point. The last triple point, namely the upper white star in Fig. 1A, is at  $\{J_{zz} = 3, J_{\pm\pm} = \frac{1}{2}, J_{\pm\pm\pm} = 1\}$ —which we refer to as the DQQ\* model, is dual to the aforementioned DQQ model (31, 32), with both models having identical thermodynamic properties, though their spin-spin correlations differ.

To begin, we first use Monte Carlo (MC) simulations to investigate in detail the thermodynamics and spin–spin correlations of the classical DQQ model, with the spins in Eq. 4 taken as classical vectors of fixed length  $|\mathbf{S}_i| = 1$ . The results are broadly summarized in Fig. 1B–F. In this figure, and throughout the paper when considering  $\mathcal{H}$  in Eq. 4, as opposed to the more general case of  $\mathcal{H}$  in Eq. 1, we fix  $D = -2J$  and measure all energies in units of  $J$  and temperature in units of  $J/k_B$ . Fig. 1B shows the temperature dependence of the specific heat,  $C$ , of the DQQ model, which exhibits a fairly sharp peak at temperature  $T^* \sim O(J \times 10^{-2})$  (note the logarithmic temperature scale in Fig. 1B), and asymptotically plateaus to a value of  $C/k_B \approx 7/8$  at the lowest temperature considered. Fig. 1C–F illustrates the evolution of the spin structure factors transverse to wave vector  $\mathbf{q}$ , as probed by unpolarized neutron scattering (19, 20, 22, and *SI*

*Appendix*), in the  $[h\ell\ell]$  and  $[hk0]$  planes for  $T > T^*$  in subpanels (C) and (D), and for  $T < T^*$  in subpanels (E and F). Here, we consider an isotropic (diagonal and unitary)  $g$ -tensor to obtain what we refer to as the “spin structure factor” (*SI Appendix*). This is in line with the approach taken in ref. 50 to expose the various features displayed by correlation functions which originate from the intertwined magnetic dipolar and electric quadrupolar degrees of freedom represented by the pseudospin components  $S^z$  and  $S^\pm$ , respectively (31). We shall discuss the experimental implications of considering the true  $g$ -tensor on the neutron structure factor of non-Kramers ion systems below in *Discussion*.

The spin–spin correlations of the DQQ model display a plethora of rich anisotropic features in  $\mathbf{q}$ -space, which are further discussed below. However, perhaps most interesting is their very rapid change when the system passes from above to below  $T^*$ . As we show next, the anisotropic features for  $T > T^*$  can be understood by considering a long-wavelength theory composed of competing rank-1 and rank-2 tensor fields, both of whose low-temperature behavior is constrained by an emergent Gauss’ law. The change in correlation functions at  $T^*$  is associated with a spin liquid to spin liquid crossover driven by entropic effects. Additionally, we will show later that this intertwined rank-1 ( $R_1$ ) and rank-2 ( $R_2$ ),  $R_1$ - $R_2$ , spin liquid phase appears to be stable in the quantum spin-1/2 case, as suggested by pseudofermion functional renormalization group (PFFRG) calculations discussed below.

**Self-Consistent Gaussian Approximation (SCGA) and Effective Long-Wavelength Theory.** The low energy configurations of the DQQ model are built from three out of the five irrep modes (42); see *SI Appendix* for more details. To further elaborate on the degeneracy of the ground-state manifold, we Fourier transform the interaction matrix in Eq. 3 to obtain  $\mathbf{M}(\mathbf{q})$ . The spectrum of this matrix displays four degenerate low-energy flat bands (*SI Appendix*) which suggests an extensively degenerate ground state manifold—a telltale sign of a CSL (11, 51). To construct an

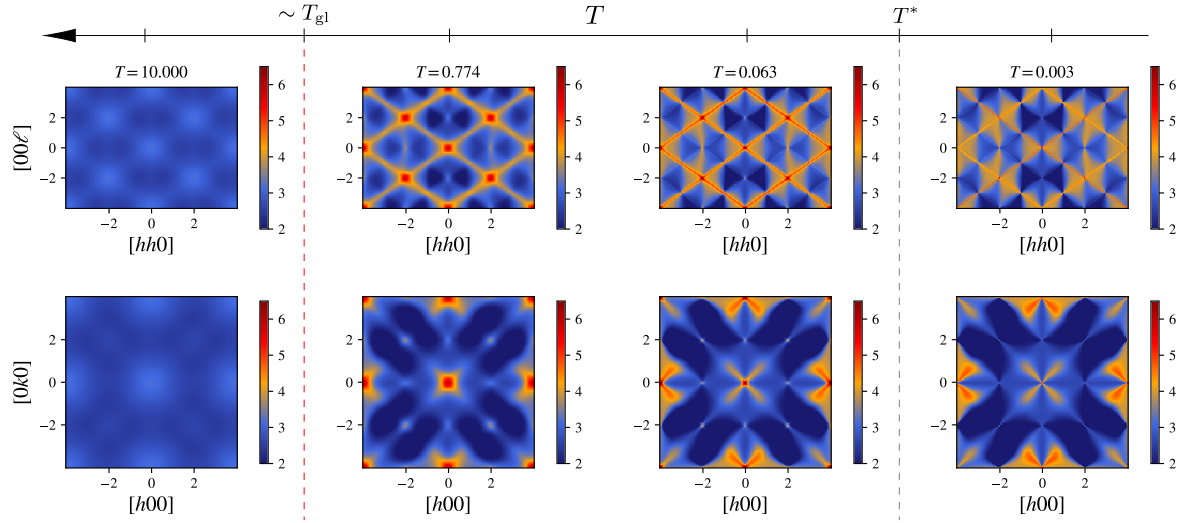


**Fig. 2.** Spin structure factors in the  $[hh\ell]$  plane (Upper row) and  $[hk0]$  plane (Lower row), obtained using a self-consistent Gaussian approximation for the temperatures illustrated above each column of figures. The red dashed line separates the gas-like (paramagnetic) regime at  $T \gtrsim T_{\text{gl}}$  from the intermediate liquid regime at  $T^* < T \lesssim T_{\text{gl}}$ . The gray line at  $T^*$  corresponds to the peak temperature of the heat capacity shown in Fig. 1A.

effective low-energy theory, we apply a SCGA, an approach proven useful in previous studies of CSLs (22, 48, 52, 53).

The spin correlation functions obtained through an SCGA analysis are shown in Fig. 2 for various temperatures and for both the  $[hh\ell]$  and the  $[hk0]$  scattering planes. These SCGA structure factors show a progressive evolution from high-temperatures ( $T \gg T_{\text{gl}}$ , with  $T_{\text{gl}}$  the paramagnetic (“spin gas”) to spin liquid crossover temperature), where the correlation function is nearly featureless in the paramagnetic regime, to the lower temperature spin liquid regime (e.g.,  $T \sim 0.774$ ), where sharp features have become visible. A comparison between Figs. 2 and 1C and D shows that the SCGA captures the anisotropic features observed in our MC simulations below  $T_{\text{gl}}$  and above  $T^*$ , but not below  $T^*$ . Twofold (53) and fourfold pinch points (11, 16) as well as continuous lines of scattering, dubbed pinch-lines (17, 27), can be seen in both the MC and SCGA results. More specifically, in the  $[hh\ell]$  plane in Fig. 1C twofold pinch points (at  $[hh\ell] = [220], [222], [002]$  and symmetry-related points) as well as lines of strong scattering intensity along the  $[111]$  and  $[\bar{1}\bar{1}\bar{1}]$  directions are observed. Additionally, fourfold pinch points at  $[hk0] = [000]$  are seen in the  $[hk0]$  plane in Fig. 1D. For more details, see [SI Appendix](#).

The observation of such anisotropic  $\mathbf{q}$ -space features had previously been related to underlying emergent gauge symmetries. Twofold pinch points are indicative of a divergence-free constraint for a vector field (14), while the fourfold pinch points and lines are related to the emergence of a rank-2 tensor field with an associated Gauss’ law constraint (16, 17). The agreement between the SCGA and the MC structure factors *above*  $T^*$  motivates the construction of an effective long-wavelength theory that we present next. On the other hand, the clear discrepancy between the SCGA and the MC structure factors for  $T < T^*$  implies that the behavior in the lowest temperature regime requires a theory that goes beyond SCGA, which we shall discuss later.

To begin, we note that Monte Carlo simulations reveal that the two high-energy  $A_2$  and  $T_2$  irreps begin to depopulate at  $T \sim O(J)$  (Fig. 3D and E), leaving only the degenerate low-energy  $T_1^{\text{lcc}}$ ,  $T_1^{\text{xy}}$  and  $E$  irreps (Fig. 3A–C) thermally populated and relevant for  $T \lesssim O(J)$ . Therefore, and similarly to the approach taken in refs. 16 and 17, we proceed to construct an effective theory for  $T > T^*$  that solely focuses on the  $T_1^{\text{lcc}}$ ,  $T_1^{\text{xy}}$

and  $E$  irreps in the temperature range  $T^* \lesssim T \lesssim T_{\text{gl}}$ . Therefore, starting from the Hamiltonian in Eq. 1, we define a rank-1 field,

$$(\mathbf{B}^{\text{lcc}})^\alpha \equiv m_{T_1^{\text{lcc}}}^\alpha, \quad [5]$$

and a rank-2 (tensor) field

$$\mathcal{M}^{\text{xy}} \equiv \sqrt{\frac{2}{3}} \begin{pmatrix} \frac{\sqrt{3}}{2} m_{\psi_2} - \frac{1}{2} m_{\psi_3} & -\frac{\sqrt{3}}{2} m_{T_1^{\text{xy}}}^z & \frac{\sqrt{3}}{2} m_{T_1^{\text{xy}}}^y \\ \frac{\sqrt{3}}{2} m_{T_1^{\text{xy}}}^z & -\frac{\sqrt{3}}{2} m_{\psi_2} - \frac{1}{2} m_{\psi_3} & -\frac{\sqrt{3}}{2} m_{T_1^{\text{xy}}}^x \\ -\frac{\sqrt{3}}{2} m_{T_1^{\text{xy}}}^y & \frac{\sqrt{3}}{2} m_{T_1^{\text{xy}}}^x & m_{\psi_3} \end{pmatrix}. \quad [6]$$

Here,  $\mathbf{B}^{\text{lcc}}$  corresponds to the fluxes in the Coulomb phase (15) (components of  $T_1^{\text{lcc}}$ ), while  $m_{T_1^{\text{xy}}}^\alpha$  are components of  $T_1^{\text{xy}}$ , while  $m_{\psi_2}$  and  $m_{\psi_3}$  are components of the  $E$  irrep ([SI Appendix](#)). In passing, we note that the rank-1 field  $\mathbf{B}^{\text{lcc}}$  and rank-2  $\mathcal{M}^{\text{xy}}$  field are uniquely composed by the local- $z$  and local- $xy$  degrees of freedom of the spins, respectively. With these, the long-wavelength approximation to the SCGA Hamiltonian reads (see [SI Appendix](#))

$$\beta\mathcal{H} = \beta E_0 + \frac{3}{16} \beta J \int d^3 \mathbf{q} \left( |\mathbf{q} \cdot \mathbf{B}^{\text{lcc}}|^2 + |\mathbf{q}^T \mathcal{M}^{\text{xy}}|^2 \right) + \lambda \int d^3 \mathbf{q} \left( |\mathbf{B}^{\text{lcc}}|^2 + \text{Tr} \left[ (\mathcal{M}^{\text{xy}})^T \mathcal{M}^{\text{xy}} \right] \right) + O(\mathbf{q}^4). \quad [7]$$

This Hamiltonian consists of three terms: The first term,  $E_0$ , denotes the ground state energy of the three degenerate irrep modes. The second term is composed of two emergent Gauss’ laws: one for the vector field  $\mathbf{B}^{\text{lcc}}$  and another for the rank-2 field  $\mathcal{M}^{\text{xy}}$ , which in the limit  $T \rightarrow 0$  correspond to  $\mathbf{q} \cdot \mathbf{B}^{\text{lcc}} = 0$  and  $\mathbf{q}^T \mathcal{M}^{\text{xy}} = 0$  and, in direct space,  $\nabla \cdot \mathbf{B}^{\text{lcc}} \equiv \partial_\alpha (\mathbf{B}^{\text{lcc}})^\alpha = 0$  and  $\partial_\alpha (\mathcal{M}^{\text{xy}})^{\alpha,\beta} = 0$ , with an implicit sum over repeated indices. The third term proportional to  $\lambda$  corresponds to the spin-length constraint in the SCGA approximation ([SI Appendix](#)).

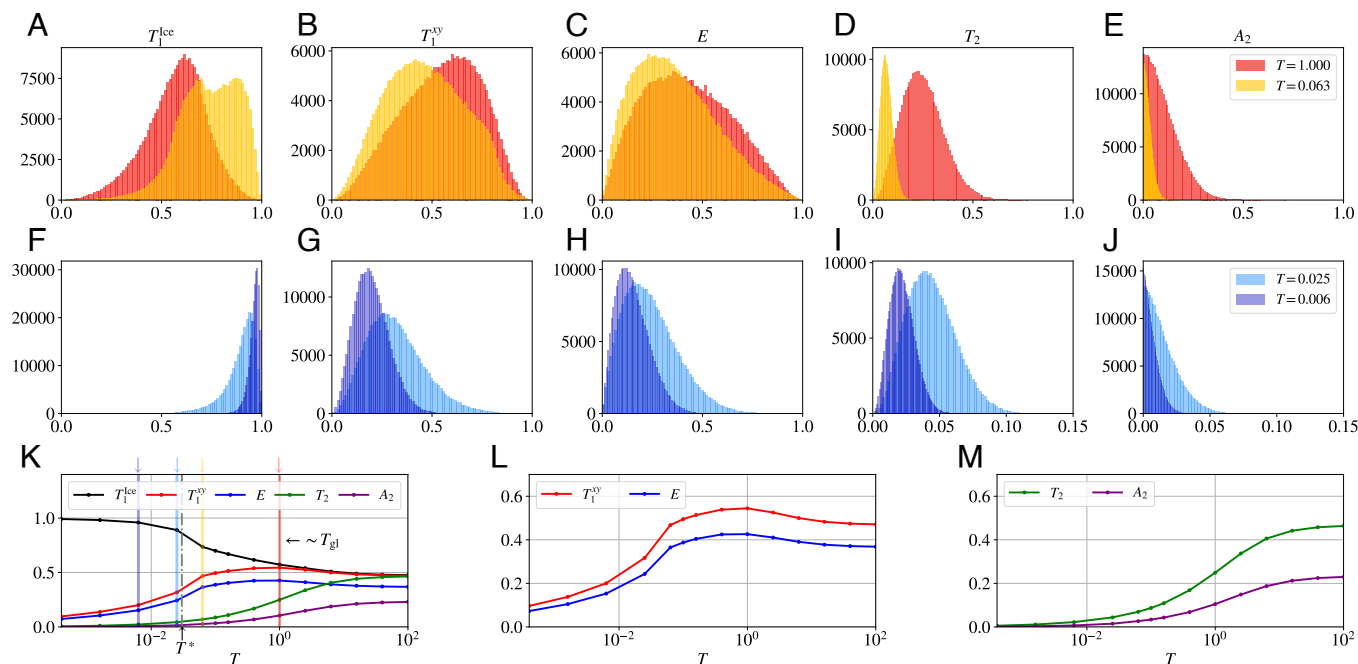


**Fig. 3.** (A–J) Distribution of the irrep mode magnitude of all the up tetrahedra ( $\{|m_l^{\hat{\alpha}}|\}$ ) of 250 Monte Carlo sampled configurations for a system size  $L = 10$  at the temperatures indicated in the rightmost panel. Each column of panels (A–J) corresponds to the distribution of a given irrep, namely, from *Left to Right*, the  $T_1^{\text{lce}}$ , the  $T_1^{\text{xy}}$ , the  $E$ , the  $T_2$ , and the  $A_2$  irreps. (K–M) Evolution of the average irrep mode magnitude,  $\frac{1}{L^3} \langle \sum_{\hat{\alpha}} |m_l^{\hat{\alpha}}| \rangle$ , on a lattice as a function of temperature averaged over 2,500 configurations sampled through Monte Carlo. The vertical shaded lines indicate the temperatures where the configurations used to produce the histograms in the first and second rows were sampled from. In subpanel (K), we identify the gray dashed-dotted line with the liquid-to-liquid crossover temperature  $T^*$ , and the red vertical line at the temperature  $T = 1.0$ , with the approximate liquid-to-gas crossover temperature  $T_{\text{gl}}$ . We note that at low temperatures the average irrep mode magnitude corresponding to the  $T_1^{\text{lce}}$  irrep approaches unity elucidating a selection of configurations with this irrep mode over configurations composed of the other two low-energy degenerate  $xy$  ( $T_1^{\text{xy}}$  and  $E$ ) irreps.

The terms corresponding to the local- $z$  spin components, i.e., those with the vector field  $\mathbf{B}^{\text{lce}}$ , describe an effective Coulomb phase where a divergence-free condition results in the twofold pinch points (46, 54). The terms describing the divergence-free condition of the local- $xy$  components, i.e., on the  $\mathcal{M}^{\text{xy}}$  tensor field, lead to fourfold pinch points in the  $[hk0]$  plane (55). Thus, the full set of anisotropic features observed in the spin structure factors along with the effective theory in Eq. 7 imply the existence of two sets of emergent gauge fields constrained by their respective Gauss' law. We thus identify the spin liquid state in the intermediate temperature regime  $T^* \lesssim T \lesssim T_{\text{gl}}$  as a rank-1—rank-2 (henceforth  $R_1$ - $R_2$ ) spin liquid.

For  $T < T^*$ , some of the anisotropic features in the spin structure factor disappear entirely, implying that a different long-wavelength theory is needed in that regime. We note that spin structure factors for  $T < T^*$  are spin-ice-like where only twofold (22, 53) pinch points are seen. Hence, we expect the  $T < T^*$  theory to resemble the Coulomb phase theory with a single Gauss' law on a (rank-1) vector field (15, 22). Indeed, such a theory will result if the  $\mathcal{M}^{\text{xy}}$  tensor field, and consequently the  $T^{\text{xy}}$  and  $E$  irreps, were to thermally depopulate (freeze-out) faster than the  $T^{\text{lce}}$  irrep due to missing higher-order gradient terms which should be incorporated in Eq. 7. As way of confirming this expectation, the depopulation of the  $T_1^{\text{xy}}$  and  $E$  irreps for  $T < T^*$  can be seen in the MC data of Fig. 3 G and H, with the distribution of all irrep projections below  $T^*$  shown in Fig. 3 F–J. The depopulation of  $T_1^{\text{xy}}$  and  $E$  irreps implies that low-temperature spin configurations for  $T < T^*$  are solely made up of  $T_1^{\text{lce}}$ , as observed in Fig. 3F. As an overview, we present in Fig. 3 K–M the average value of each irrep projection

as a function of temperature. To summarize, two regimes below  $T_{\text{gl}}$ , separated by the crossover temperature  $T^*$ , can be identified: one where  $T_1^{\text{lce}}$ ,  $T_1^{\text{xy}}$ , and  $E$  irreps have similar average values ( $T^* \lesssim T \lesssim T_{\text{gl}}$ ), and another ( $T \lesssim T^*$ ) where all irreps but  $T_1^{\text{lce}}$  are thermally depopulated.

We now discuss the mechanism for the depopulation of  $T_1^{\text{xy}}$ , and  $E$  irreps, and the thermal crossover between the two spin liquid phases. The value of the specific heat plateau at low temperatures in Fig. 1B, namely,  $C/k_B \sim 7/8 = 0.875$ , and not 1 as expected from the equipartition theorem, already hints at what is the mechanism at play (46, 56). Specifically, it suggests that low-energy excitations above the ground state are not all quadratic, but that higher-order fluctuation modes are being thermally excited. To confirm this, we investigate the low energy spin fluctuations about individual ground state configurations through a classical low-temperature expansion (CLTE).

### Classical Low-Temperature Expansion: Entropic Selection of the Rank-1 Spin Liquid.

By borrowing the method from ref. 57, we numerically construct a CLTE which yields a quadratic theory of spin fluctuations in real-space about a ground-state configuration. The spin-fluctuation modes and their corresponding energies are identified as the eigenmodes and eigenvalues of the (quadratic spin-fluctuation) Hessian matrix (*SI Appendix*). In this approach, quartic and higher-order modes show up as zero modes as the quadratic CLTE theory does not contain higher-order spin fluctuations terms (*SI Appendix*). This observation therefore allows us to quantify the fraction of higher-order spin-fluctuating modes by tracking the number of quadratic zero modes identified in this theory.

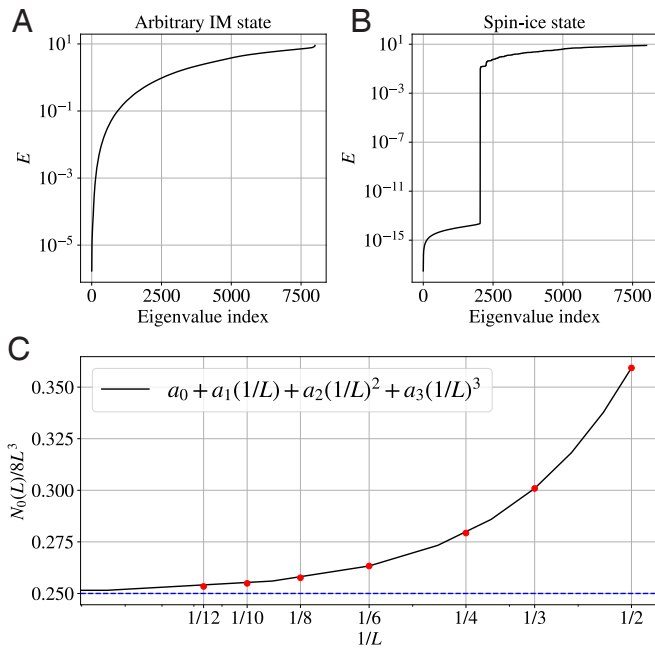


**Fig. 4.** Energy eigenvalues of the spin fluctuation modes obtained from a real space CLTE where the ground-state configurations are a minimum energy configuration obtained through IM (A), and a spin-ice configuration obtained via classical Monte Carlo on an Ising AFM model (B), both states were obtained for a system size of  $L = 10$ . In these plots, the  $x$  axis labels the numbered eigenvalue index, ranging from 1 to 8,000, and the  $y$  axis labels the energy of the eigenvalues. (C) Evolution of the fraction of zero-mode eigenvalues about a spin-ice configuration for system size  $L \in \{2, 3, 4, 6, 8, 10, 12\}$  averaged over 100 spin-ice configurations. Here, the black line is a third order in  $1/L$  polynomial fit to the data where  $a_0 \sim 0.25$ .

As discussed above, the depopulation of the  $E$  and the  $T_1^{xy}$  irreps and the increasing population of the  $T_1^{1cc}$  irrep below  $T^*$  implies the selection of spin-ice configurations at low temperatures; see Fig. 3. To expose the driving mechanism behind this selection, we apply the real-space CLTE to two types of spin configurations: i) to various pure spin-ice configurations (where all spins are constrained to point along their local  $z$  axis) and ii) to numerically obtained non-spin-ice ground state configurations (where the spins are not constrained to point along the local- $z$  axis). These two sets of configurations are respectively obtained by employing classical Monte Carlo simulations on an Ising antiferromagnetic model for the spin-ice configurations, and a numerical iterative energy minimization (IM) directly at  $T = 0$  (obtained with the maximal numerical accuracy that we could afford) for non-spin-ice configurations (SI Appendix). Both the IM and the pure spin-ice configurations are obtained for a system of linear size  $L = 10$ .

Fig. 4 A and B depict the energy eigenvalues obtained from a CLTE where the starting ground-state is (A) a configuration obtained via IM and (B) perfect spin-ice configuration. For the configuration obtained via IM, the energy spectrum in Fig. 4A shows a continuous progression of energy eigenvalues with the smallest eigenvalues of order  $O(J \times 10^{-5})$ . In contrast, for the spin-ice configuration, the energy spectrum illustrated in Fig. 4B shows a sudden drop and a significant fraction of eigenvalues with energy below  $O(J \times 10^{-11})$ . We identify these as zero modes within the quadratic theory. The comparison of the two spectra along with the monotonous thermal depopulation of the  $E$  and  $T_1^{xy}$  irreps indicate that spin fluctuations about a spin-ice configuration are softer than those about a non-spin-ice configuration implying that spin-ice configurations possess a higher entropy (lower free-energy) than the non-spin-ice

states obtained through IM, resulting in their selection at low temperatures. While the spectra presented in Fig. 4 A and B are only shown for two unique configurations, we have carried out the analysis for about 100 different IM and pure spin-ice configurations and obtained quantitatively equivalent energy spectra distributions.

To find the fraction of quartic modes about a spin-ice configuration, we count the number of vanishing energy eigenvalues (we identify an eigenvalue with a zero-mode if its numerical value is below  $J \times 10^{-9}$ ) and study how the fraction of these evolves as a function of system size  $L$ . We fit the number of zero eigenvalues as a function of  $L$  using the following form

$$N_0(L) = 8L^3(a_0 + a_1/L + a_2/L^2 + a_3/L^3), \quad [8]$$

where  $a_0$ ,  $a_1$ ,  $a_2$ , and  $a_3$  correspond to the fraction of zero eigenvalues originating from local, one-dimensional, two-dimensional, and global zero modes, respectively. We consider system sizes  $L = \{2, 3, 4, 6, 8, 10, 12\}$ , calculate the fraction of zero eigenvalues, i.e.,  $N_0(L)/8L^3$ , and plot it as a function of  $L$ . As seen in Fig. 4C, this fraction of zero eigenvalues approaches very precisely  $1/4$  as the system size approaches the thermodynamic limit,  $1/L \rightarrow 0$ .

This fraction of zero quadratic modes is independently confirmed by the aforementioned observed value of the specific heat  $C/k_B \approx 7/8$  at low temperatures. This result suggests that  $3/4$  of the modes are quadratic whereas the remaining  $1/4$  are quartic, with  $C = (n_2 k_B/2 + n_4 k_B/4)/N_s$ , where  $N_s = 4$  is the number of spins per tetrahedron, and  $n_2 = 6$  and  $n_4 = 2$  are numbers of quadratic respectively (46, 56), giving  $C/k_B = 7/8$ .

To summarize, our MC analysis shows no evidence for a symmetry-breaking transition down to zero temperature. Rather, it identifies a  $R_1$ - $R_2$  spin liquid state that develops upon cooling from the paramagnetic phase and which is followed upon further cooling by a crossover to a spin-ice-like spin liquid at a temperature  $T^*$ . The CLTE analysis implies that the thermal crossover at the temperature  $T^*$  and, therefore, the selection of the low-temperature spin-ice-like spin liquid in the DQQ model proceeds via an entropic mechanism. While this mechanism is similar to an order-by-disorder selection of a magnetically ordered state in a degenerate manifold (42, 58), for the DQQ model, the selection does not result in a magnetically ordered state. To the best of our knowledge, this finding constitutes the first observation of a classical temperature-driven “disorder-by-disorder” mechanism where an extensively degenerate submanifold is selected by thermal fluctuations.

**Quantum Spin-1/2 Model.** We now turn to the corresponding quantum spin-1/2 version of the DQQ model to investigate how quantum fluctuations modify our findings for the classical system. We perform this study in an extended parameter regime of the exchange constants  $J_{zz}$ ,  $J_{\pm}$ ,  $J_{\pm\pm}$ , varying them in the vicinity of the DQQ point ( $J_{zz} = 3$ ,  $J_{\pm} = \frac{1}{2}$ ,  $J_{\pm\pm} = -1$ ). This non-Kramers Hamiltonian with positive  $J_{zz}$  has been studied before by both quantum and classical methods (30, 31, 40, 43, 44). The classical model at  $T = 0$  shows the four phases of Fig. 1A (three quadrupolar phases associated with the irreps  $E$ ,  $T_2$ ,  $T_1^{xy}$  and one dipolar phase with the irrep  $T_1^{1cc}$ ). The most striking observation in studies of the quantum spin-1/2 model is the replacement of the classical spin-ice phase by a U(1) quantum spin liquid in the vicinity of the Ising point  $J_{\pm} = J_{\pm\pm} = 0$  (7, 44).

We first apply the PFFRG method (59, 60) to compute the  $T = 0$ , spin-1/2 phase diagram of the non-Kramers

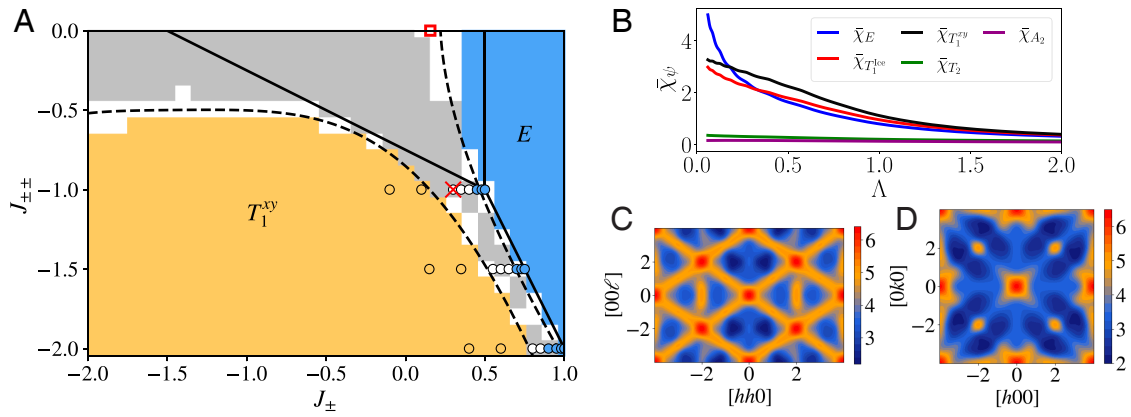


**Fig. 5.** (A) PFFRG ground state phase diagram of the spin-1/2 non-Kramers pyrochlore model at  $T = 0$  with fixed  $J_{zz} = 3$ , where the gray region denotes an absence of magnetic long-range order, the yellow and blue regions correspond to the  $\mathbf{q} = \mathbf{0}$  quadrupolar orders  $T_1^{xy}$  and  $E$ , respectively, and the white regions are of uncertain magnetic behavior. As a guide to the eye, the approximate quantum phase boundaries from PFFRG are indicated by dashed lines. Solid black lines mark the classical phase boundaries which meet at the DQQ point ( $J_{zz} = 3, J_{\pm} = \frac{1}{2}$  and  $J_{\pm\pm} = -1$ ). The HTSE results are shown as circles whose colors correspond to the order parameter susceptibility dominating in a calculation up to order  $1/T^8$ . The phase boundary between quantum spin ice and magnetic  $E$  phases, as previously determined by quantum Monte Carlo on the unfrustrated  $J_{\pm\pm} = 0$ -line (the so-called XXZ model) is marked by a red square (44). (B) Order parameter susceptibilities  $\bar{\chi}_{\psi}$  from PFFRG at  $T = 0$  as a function of the renormalization group parameter  $\Lambda$  for the quantum spin-1/2 model with interactions  $\{J_{zz}, J_{\pm}, J_{\pm\pm}\} = \{3.0, 0.3, -1.0\}$ , marked by a red cross in the phase diagram in (A). (C and D) Static (zero frequency) spin structure factors from PFFRG at  $T = 0$  for the same model as in (B) within the  $[hh\ell]$  and  $[hk0]$  planes in the low-cutoff limit  $\Lambda \rightarrow 0$ .

model, shown in Fig. 5A, focusing on the parameter region around the DQQ point. This method determines magnetic ordering via the presence of an RG flow breakdown of the cutoff-dependent susceptibility (SI Appendix). The nature of the magnetic order is further determined by the dominant order parameter susceptibility  $\bar{\chi}_{\psi}$  defined by

$$\bar{\chi}_{\psi} = \frac{1}{N} \sum_{ij} \sum_{\alpha\beta} \mathbf{n}_i^{\alpha} \bar{\chi}_{ij}^{\alpha\beta} \mathbf{n}_j^{\beta}, \quad [9]$$

where the vectors  $\mathbf{n}_i$  describe fixed spin orientations on all sites  $i$  corresponding to the classical magnetic order  $\psi$  being probed (42). We take the orders  $\psi$  from our irrep analysis, i.e., they are of  $E, T_1^{xy}, T_1^{ice}, A_2$ , or  $T_2$  type. Note that the order parameter susceptibilities corresponding to different  $\mathbf{q} = \mathbf{0}$  spin configurations within the same irrep are identical (42). Note that in Eq. 9,  $\bar{\chi}_{ij}^{\alpha\beta} \equiv \int_0^{\infty} d\tau \langle S_i^{\alpha}(\tau) S_j^{\beta}(0) \rangle$  is the static spin correlation function computed in imaginary time domain  $\tau$ .

The quantum ground state phase diagram in Fig. 5A determined using PFFRG shows distinct differences from the classical one in Fig. 1A: i) The paramagnetic (gray) domain extends its regime of stability, expanding into the region of classical  $T_1^{xy}$  order. ii) The extent of the  $E$  long-range ordered phase is enhanced by quantum fluctuations and partially penetrates the paramagnetic (spin ice) region of the classical model, in agreement with a previous quantum Monte Carlo study considering  $J_{\pm\pm} = 0$  (44). iii) These phase boundary shifts caused by quantum fluctuations create a characteristic narrow corridor of quantum paramagnetic behavior approximately parallel to the classical  $E$ - $T_1^{xy}$  phase boundary.

The distinction between magnetic order and quantum paramagnetic behavior via a flow breakdown of susceptibilities is subject to uncertainties in PFFRG especially along the phase boundaries. As shown in Fig. 5A, the quantum DQQ model lies in such a region of uncertainty. Although the unambiguous identification of magnetic order with PFFRG is not possible in this region, we observe a comparatively large  $\bar{\chi}_E$  order parameter susceptibility (SI Appendix) indicating strong  $E$ -type spin correlations in the quantum DQQ model at  $T = 0$ . This is in stark

contrast to the classical DQQ model which shows dominant spin-ice correlations in the low temperature limit. However, we find that for coupling parameters deeper in the quantum paramagnetic corridor, but still close to the DQQ point, some of our observations from the classical DQQ model are recovered. Specifically, by visual inspection, we observe matching spin structure factor patterns of the quantum non-Kramers model around  $\{J_{zz}, J_{\pm}, J_{\pm\pm}\} = \{3.0, 0.3, -1.0\}$  for  $T = 0$  and that of the classical DQQ model at  $T \gtrsim T^*$ , compare Fig. 5C with Figs. 1C and 5D with Fig. 1D. The fact that this agreement holds only when the classical model is considered in the intermediate ( $T^* \lesssim T \lesssim T_{gl}$ ) temperature regime where the  $R_1$ - $R_2$  phase is realized suggests that no corresponding entropic selection mechanism occurs in the quantum model at  $\{J_{zz}, J_{\pm}, J_{\pm\pm}\} = \{3.0, 0.3, -1.0\}$  as is observed in the classical model as  $T \rightarrow 0$  at the DQQ point (see Fig. 3). This is further confirmed by the renormalization group flows of order parameter susceptibilities  $\bar{\chi}_{\psi}$ , shown in Fig. 5B, where  $\bar{\chi}_E, \bar{\chi}_{T_1^{xy}}$ , and  $\bar{\chi}_{T_1^{ice}}$  are all of similar size for  $\{J_{zz}, J_{\pm}, J_{\pm\pm}\} = \{3.0, 0.3, -1.0\}$  at  $T = 0$ . Note, however, that  $\bar{\chi}_{T_1^{ice}}$  only takes into account the  $\mathbf{q} = \mathbf{0}$  spin ice configurations and thus does not represent the full spin ice manifold. All these observations lend support to the conclusion that in this corridor with paramagnetic behavior, an exotic quantum spin liquid described by coexisting emergent rank-1 and rank-2 gauge fields may exist. On the other hand, it is strongly believed that the XXZ model in the  $0 < J_{\pm} \lesssim 0.156$  window on the  $J_{\pm\pm} = 0$  axis hosts a U(1) spin liquid (44). It is likely that this phase somewhat extends over a finite  $|J_{\pm\pm}| \neq 0$  range. Thus, our results beg the question whether there is a quantum spin liquid to quantum spin liquid transition as the DQQ point is approached from above (i.e., from the  $J_{\pm\pm} = 0$  axis and  $J_{\pm}$  becoming negative in Fig. 5A).

To corroborate these observations with a complementary method, we next discuss the results of a high-temperature series expansion (HTSE) study, whose details can be found in the SI Appendix. We calculate the susceptibilities for both the  $T_1^{xy}$  and  $E$  order parameters, focusing on the coupling regime where PFFRG identified a paramagnetic corridor. The first-order HTSE for the inverse susceptibility gives the Curie–Weiss law (taking the zeroth order term as the single-spin Curie term). We find that the Curie–Weiss temperature for the  $T_1^{xy}$  and  $E$  order parameters

exchange their dominance upon crossing the classical  $T_1^{xy} - E$  phase boundary. This shows the equivalence of classical and quantum models at the Curie–Weiss (mean-field) level.

Higher orders of the expansion are analyzed by Padé approximants (61) and show the following: The  $E$  susceptibility dominates along the classical  $E-T_1^{xy}$  phase boundary and, to some degree, in the classical  $T_1^{xy}$  phase. The blue circles in Fig. 5A mark regions where the  $E$  susceptibility grows rapidly upon decreasing temperature, while the orange circles show regions where the  $T_1^{xy}$  susceptibility grows faster. The parameter regions where the  $T_1^{xy}$  and  $E$  susceptibilities dominate, respectively, agree well with the PFFRG results. In between these  $T_1^{xy}$  and  $E$  regions, HTSE finds a corridor running parallel to the classical  $E-T_1^{xy}$  phase boundary, but shifted inside the classical  $T_1^{xy}$  phase where neither susceptibility is found to grow substantially, again very similar to the paramagnetic strip found in PFFRG (see *SI Appendix* for more details). Altogether, these results imply the exciting possibility of an extended quantum spin liquid region near the DQQ point, and potentially exhibiting an  $R_1$ - $R_2$  gauge structure as suggested on the basis of the classical theory.

## Discussion

The prevalence of different gauge theories on different energy scales is a well-known feature of the standard model of high-energy physics, which comprises U(1), SU(2), and SU(3) gauge structures that produce distinct physical properties, e.g., on typical atomic and nuclear energy scales. In this paper, we have used the concept of coexisting gauge theories associated with different energy scales in a condensed matter system. More precisely, the system we investigated is a Heisenberg plus Dzyaloshinskii–Moriya interaction model on the pyrochlore lattice in the vicinity of the classical multiphase triple point  $D/J = -2$ . At the classical level, the multiphase point has been studied by a comprehensive set of numerical and analytical methods and found to exhibit several unique features. There are two distinct spin liquid phases as a function of temperature with no signal of a symmetry-breaking transition down to the lowest temperatures. The two spin liquid phases uncovered are described by different effective low-energy gauge theories with a sharp crossover between the two that is signaled by a peak in the specific heat. The higher temperature spin liquid phase is a  $R_1$ - $R_2$  spin liquid that exhibits both two-fold and four-fold pinch points in the spin structure factors and is described by fluctuating rank-1 vector and rank-2 tensor fields.

The lower temperature spin liquid, which persists down to  $T = 0$ , is a spin-ice-like Coulomb phase whose emergence from the higher temperature phase is an illustration of entropic “disorder-by-disorder” selection. For the manifold of states selected at low temperatures, a fraction of the eigenmodes have zero energy at the quadratic level. This gives them an entropic advantage and is also responsible for reducing the low-temperature heat capacity below the standard equipartition  $C/k_B = 1$  value assuming solely quadratic-level spin fluctuations.

Our study of the quantum model using PFFRG shows that phase boundaries are renormalized by quantum fluctuations, with the best match between the classical and quantum spin–spin correlations realized slightly away from the  $D/J = -2$  value. Perhaps more interestingly, we find an extended corridor in parameter space that runs parallel to the classical phase boundary between the  $T_1^{xy}$  and  $E$  phases, where the ground state remains nonmagnetic. These results are further supported

by high-temperature series expansion calculations for different order-parameter susceptibilities.

The full anisotropic features of the spin–spin correlations are needed to distinguish between the two spin-liquid phases. The use of isotropic  $g$ -factors was essential to expose this difference in a compact manner. In non-Kramers spin systems, coupling to time-reversal odd fields such as external magnetic fields or neutron spin requires  $g^{zz} \neq 0$ ,  $g^{xx} = g^{yy} \equiv g^\perp = 0$  (31, 32). Structure factors obtained with these anisotropic  $g$ -factors fail to distinguish between the two phases (*SI Appendix*). This means that experimental elucidation of the two spin-liquids and the transition between them would pose new challenges, but which could possibly be tackled by studying response to strain fields (62).

From a materials perspective, a previous work (40) suggested that the perplexing  $\text{Tb}_2\text{Ti}_2\text{O}_7$  pyrochlore antiferromagnet (32, 39), or its  $\text{Tb}_{2+x}\text{Ti}_{2-x}\text{O}_7$  off-stoichiometry variant, may be located in the vicinity of the DQQ\* point we identified in this work. Our results provide an enlarged and intriguing perspective as to the exotic physics at play in these compounds, namely that they may reside in a region of spin–spin coupling parameters near the DQQ\* point, dual to the DQQ point where quantum spin-liquidity is observed in Fig. 5A.

Our investigation raises several questions that should be addressed in the future: i) Is the low-temperature spin-ice phase near the DQQ point continuously connected to the U(1) quantum spin ice (7) spin liquid around the Ising model? If not, is it possible to observe a transition by continuously tuning the interaction couplings as was predicted for other similar systems (33, 34). ii) Are there emergent U(1) photons in this phase and what signatures do they have? iii) How could one experimentally investigate the dynamical pseudospin structure factors associated with nondipolar degrees of freedom?

Finally, the results presented in this paper are a further reminder of the richness of collective phenomena that frustrated spin systems harbor, creating “their own” nanoscale structure of effective degrees of freedom and driving distinct thermal and quantum regimes of spin liquidity. Intriguingly, this is akin to the local tetrahedral bonding arrangement that some compounds, such as phosphorous, sulfur, and silicon possess in their liquid state and which is thought to play an essential role in the liquid-to-liquid transition they display (36, 37).

## Methods

**Irreducible Representation Analysis.** As was noted in ref. 41, the most general nearest-neighbor bilinear pyrochlore Hamiltonian can be written as the sum of single up and down tetrahedra Hamiltonians

$$\mathcal{H} = \sum_{\boxtimes} \mathcal{H}^{\boxtimes}, \quad [10]$$

where  $\mathcal{H}^{\boxtimes}$  can be decomposed into its irreducible representations (irreps) (*SI Appendix*); see Eq. 3 above, where the weights  $a_l$  are smooth linear functions of the nearest-neighbor interaction couplings  $\{J_{ZZ}, J_{\pm\pm}, J_{\pm\pm\pm}, J_{\pm\pm\pm}\}$  (41, 63) and  $m_l^{\boxtimes}$  are the corresponding irrep fields onto which the spin configuration for tetrahedron  $\boxtimes$  can be decomposed. The irrep analysis can be used as a first approximation in the prediction of a long-range ordered phase (41, 42) as well as the building blocks in the construction of an effective long-wavelength theory for systems that avoid long-range order (*SI Appendix*).

**MC Simulations.** MC simulations were performed on systems of size  $L \in \{6, 8, 10, 12\}$ , corresponding to  $4L^3$  classical spins with  $|\mathbf{S}_i| = 1$ , where we used  $5 \times 10^4$  thermalization sweeps and  $8 \times 10^4$  measurement sweeps. For each sweep, the system was updated using a Gaussian update (64), overrelaxation



(65, 66), and a loop algorithm for Heisenberg spins which was inspired by refs. 67 and 68, where a single loop is attempted to be both identified and flipped per sweep. Additionally, we performed an average over 500 independent MC simulations.

We also implemented a classical Ising MC with single spin-flip updates supplemented with a loop algorithm to sample the perfect spin-ice configurations of system size  $L \in \{2, 3, 4, 6, 8, 10, 12\}$  used in the analysis of the classical low-temperature expansion.

**SCGA.** The SCGA (22, 48, 52) is a classical approximation where the spin-length constraint is replaced by a soft-spin constraint where the spin length is preserved on average over the whole system. In other words, for an  $n$ -component spin, the spin-length constraint,  $\sum_{\alpha=1}^n (S^\alpha)^2 = |\mathbf{S}|^2 = S^2$ , is replaced by the thermodynamic average condition  $\langle |\mathbf{S}|^2 \rangle = S^2$ . To compare our results with the MC simulations, we take  $S = 1$ . This condition is enforced by the introduction of a Lagrange multiplier  $\lambda$  imposing the average constraint at all temperatures. The introduction of this approximation in the spin-length constraint results in a quadratic (Gaussian) theory which can be solved numerically exactly, and from which quantities such as the spin-spin correlation functions can be computed (SI Appendix).

**Classical Low-Temperature Expansion.** A classical low-temperature expansion is a framework where a low-energy Hamiltonian describing the fluctuations about a low-temperature state is derived. Such Hamiltonian can be obtained for the general bilinear spin Hamiltonian (SI Appendix) by assuming that the spin components are described in a local orthonormal frame where the (local)  $\tilde{z}_i$  axis is along the zero-temperature orientation of the spin  $\mathbf{S}_i$  at a given pyrochlore lattice site  $i$ . This allows us to write the spin at FCC site  $i$  and sublattice  $a$  as,

$$\mathbf{S}_{ia} \simeq \left( \delta n_{ia'}^{\tilde{x}}, \delta n_{ia'}^{\tilde{y}}, S \left( 1 - \frac{(\delta n_{ia'}^{\tilde{x}})^2}{2S^2} - \frac{(\delta n_{ia'}^{\tilde{y}})^2}{2S^2} \right) \right), \quad [11]$$

where it is assumed that the system displays small fluctuations  $\delta n_{ia}^\alpha$  about the low-temperature spin orientation, where  $\alpha$  labels the perpendicular directions to the low-temperature spin orientation with  $|\delta n^\alpha| \ll S$ , where we take  $S = 1$ .

**PFFRG.** In PFFRG, the spins are first mapped onto pseudofermions which allows one to study quantum spin models at  $T = 0$  within the functional renormalization group formalism (59, 60). After introducing an infrared frequency cutoff parameter  $\Lambda$  in the fermionic propagator, coupled differential equations for the fermionic vertex functions are solved from the known high-energy limit  $\Lambda \rightarrow \infty$  toward the cutoff-free model  $\Lambda \rightarrow 0$ . The computed  $\Lambda$ -dependent susceptibility reveals whether a model is magnetically ordered or quantum paramagnetic. Because of the approximations involved, a magnetic order transition usually does not result in a divergence of the susceptibility, but rather in a flow breakdown manifested by a kink. In contrast, a quantum paramagnetic susceptibility flow remains smooth down to the cutoff-free limit  $\Lambda \rightarrow 0$ .

We apply the one-loop plus Katanin PFFRG method (59, 60) with an exponential frequency mesh, containing  $32^3 (1,000)$  positive frequencies for the fermionic two-particle vertex (self-energy). Spin correlations, spanning beyond a distance of four nearest-neighbor distances, are approximated to be zero (no periodic boundary conditions are applied). The flow equations are solved using an explicit embedded Runge-Kutta [2, 3] method with adaptive step size (69).

**High-Temperature Series Expansion.** The high-temperature series expansion method is based on expanding the Boltzmann weight  $\exp(-\beta\mathcal{H})$  in powers of the inverse temperature  $\beta \equiv 1/T$ ,

$$\exp(-\beta\mathcal{H}) = \sum_n \frac{(-\beta\mathcal{H})^n}{n!}. \quad [12]$$

High-temperature series expansion for an extensive property  $P$  can be calculated by a linked-cluster method (61),

$$\frac{P}{N_s} = \sum_c L(c) \times W(c), \quad [13]$$

where  $N_s$  is the number of spins, and the sum is over all linked or connected clusters that can be embedded in the lattice. The quantity  $L(c)$ , called the lattice constant, is the number of ways the cluster  $c$  can be embedded in the lattice per lattice site. The quantity  $W(c)$ , called the weight of the cluster, can be obtained from a high-temperature series expansion for some physical property  $P$  for the cluster  $c$ ,  $P(c)$ , from the relation

$$P(c) = \sum_{s \subseteq c} W(s), \quad [14]$$

where the sum is over all subclusters of the cluster  $c$  including the cluster  $c$ . Thus, starting with the smallest cluster, one can calculate the weight of all clusters up to some order. One can show that if all clusters of up to  $n$  bonds are included in the sum in Eq. 13, it gives the high-temperature series expansion for the infinite system to order  $\beta^n$ .

We have used the high-temperature series expansion method to calculate order-parameter susceptibilities for  $T_1^{xy}$  and  $E$  order parameters (SI Appendix).

**Data, Materials, and Software Availability.** Data in addition to those presented in the main text and in the SI Appendix, along with computer codes developed for the present study, are available in the following database: [https://github.com/daniel-lozano/R1R2\\_spin\\_liquid\\_data](https://github.com/daniel-lozano/R1R2_spin_liquid_data) (70).

**ACKNOWLEDGMENTS.** We acknowledge useful discussions with Kai Chung, Alex Hickey, and Peter Holdsworth. The work at the University of Waterloo was supported by the Natural Sciences and Engineering Research Council of Canada and the Canada Research Chair (Tier 1, M.J.P.G.) program. Numerical simulations done at Waterloo were performed thanks to the computational resources of the Digital Research Alliance of Canada. D.L.-G. acknowledges the computing time provided by the Digital Research Alliance of Canada and the financial support from the Deutsche Forschungsgemeinschaft through the Hallwachs-Röntgen Postdoc Program of the Würzburg-Dresden Cluster of Excellence on Complexity and Topology in Quantum Matter-*ct.qmat* (EXC 2147, project-id 390858490) and through Sonderforschungsbereich 1143 (project-id 247310070). J.R. and V.N. gratefully acknowledge the computing time provided to them on the high-performance computer Noctua 2 at the Verbund für Nationales Hochleistungsrechnen Center PC2. This is funded by the Federal Ministry of Education and Research and the state governments participating on the basis of the resolutions of the Gemeinsame Wissenschaftskonferenz for the national high-performance computing at universities ([www.nhr-verein.de/unsere-partner](http://www.nhr-verein.de/unsere-partner)). Some of the computations for this research were performed using computing resources under project hpc-prf-pm2fzg. V.N. would like to thank the High Performance Computing Service of Zentraleinrichtung für Datenverarbeitung and Tron cluster service at the Department of Physics, Freie Universität Berlin, for computing time. The work of Y.I. and M.J.P.G. was performed, in part, at the Aspen Center for Physics, which is supported by NSF grant PHY-2210452. The work of R.R.P.S. was supported by the NSF grant DMR-1855111. J.O. acknowledges computing support provided by the Australian National Computation Infrastructure program. J.R. thanks Indian Institute of Technology (IIT) Madras for a Visiting Faculty Fellow position under the Institute of Eminence program. The participation of Y.I. at the Aspen Center for Physics was supported by the Simons Foundation. This research was supported in part by the NSF under Grant No. NSF PHY-1748958. Y.I. acknowledges support by the International Centre for Theoretical Physics through the Associates Programme and from the Simons Foundation through grant number 284558FY19, IIT Madras through the QuCenDIEM Centre of Excellence (Project No. SP22231244CPETWOQCDOHC), the International Centre for Theoretical Sciences (ICTS), Bengaluru, India during a visit for participating in the program "Frustrated Metals and Insulators" (Code: ICTS/frumi2022/9). Y.I. acknowledges the use of the computing resources at High Performance Computing Environment, IIT Madras.

Author affiliations: <sup>a</sup>Department of Physics and Astronomy, University of Waterloo, Waterloo, ON N2L 3G1, Canada; <sup>b</sup>Institut für Theoretische Physik und Würzburg-Dresden Cluster of Excellence ct.qmat, Technische Universität Dresden, Dresden 01062, Germany;

1. F. J. Wegner, Duality in generalized Ising models and phase transitions without local order parameters. *J. Math. Phys.* **12**, 2259–2272 (1971).
2. P. A. Lee, N. Nagaosa, X. G. Wen, Doping a Mott insulator: Physics of high-temperature superconductivity. *Rev. Mod. Phys.* **78**, 17–85 (2006).
3. X. G. Wen, *Quantum Field Theory of Many-Body Systems: From the Origin of Sound to an Origin of Light and Electrons* (Oxford University Press, 2007).
4. C. Lacroix, P. Mendels, F. Mila, *Introduction to Frustrated Magnetism* (Springer, 2011).
5. L. Balents, Spin liquids in frustrated magnets. *Nature* **464**, 199–208 (2010).
6. Y. Zhou, K. Kanoda, T. K. Ng, Quantum spin liquid states. *Rev. Mod. Phys.* **89**, 025003 (2017).
7. M. J. P. Gingras, P. A. McClarty, Quantum spin ice: A search for gapless quantum spin liquids in pyrochlore magnets. *Rep. Prog. Phys.* **77**, 056501 (2014).
8. C. Broholm *et al.*, Quantum spin liquids. *Science* **367**, eaay0668 (2020).
9. L. Savary, L. Balents, Quantum spin liquids: A review. *Rep. Prog. Phys.* **80**, 016502 (2016).
10. G. Misguich, D. Serban, V. Pasquier, Quantum dimer model on the Kagome lattice: Solvable dimer-liquid and Ising gauge theory. *Phys. Rev. Lett.* **89**, 137202 (2002).
11. O. Benton, R. Moessner, Topological route to new and unusual coulomb spin liquids. *Phys. Rev. Lett.* **127**, 107202 (2021).
12. A. Wietek, S. Capponi, A. M. Läuchli, Quantum electrodynamics in  $2 + 1$  dimensions as the organizing principle of a triangular lattice antiferromagnet. *Phys. Rev. X* **14**, 021010 (2024).
13. X. Y. Song, C. Wang, A. Vishwanath, Y. C. He, Unifying description of competing orders in two-dimensional quantum magnets. *Nat. Commun.* **10**, 4254 (2019).
14. C. L. Henley, The coulomb phase in frustrated systems. *Annu. Rev. Condens. Matter Phys.* **1**, 179 (2010).
15. C. Castelnovo, R. Moessner, S. L. Sondhi, Spin ice, fractionalization, and topological order. *Annu. Rev. Condens. Matter Phys.* **3**, 35 (2012).
16. H. Yan, O. Benton, L. D. C. Jaubert, N. Shannon, Rank-2  $U(1)$  spin liquid on the breathing pyrochlore lattice. *Phys. Rev. Lett.* **124**, 127203 (2020).
17. O. Benton, L. D. C. Jaubert, H. Yan, N. Shannon, A spin-liquid with pinch-line singularities on the pyrochlore lattice. *Nat. Commun.* **7**, 11572 (2016).
18. H. D. Zhou *et al.*, Chemical pressure effects on pyrochlore spin ice. *Phys. Rev. Lett.* **108**, 207206 (2012).
19. T. Fennell *et al.*, Magnetic coulomb phase in the spin ice  $\text{Ho}_2\text{Ti}_2\text{O}_7$ . *Science* **326**, 415–417 (2009).
20. D. J. P. Morris *et al.*, Dirac strings and magnetic monopoles in the spin ice  $\text{Dy}_2\text{Ti}_2\text{O}_7$ . *Science* **326**, 411–414 (2009).
21. C. L. Henley, Power-law spin correlations in pyrochlore antiferromagnets. *Phys. Rev. B* **71**, 014424 (2005).
22. K. T. K. Chung *et al.*, Probing flat band physics in spin ice systems via polarized neutron scattering. *Phys. Rev. Lett.* **128**, 107201 (2022).
23. D. Bergman, J. Alicea, E. Gull, S. Trebst, L. Balents, Order-by-disorder and spiral spin-liquid in frustrated diamond-lattice antiferromagnets. *Nat. Phys.* **3**, 487–491 (2007).
24. T. Mizoguchi, L. D. C. Jaubert, R. Moessner, M. Udagawa, Magnetic clustering, half-moons, and shadow pinch points as signals of a proximate Coulomb phase in frustrated Heisenberg magnets. *Phys. Rev. B* **98**, 144446 (2018).
25. F. L. Buessen, M. Hering, J. Reuther, S. Trebst, Quantum spin liquids in frustrated spin-1 diamond antiferromagnets. *Phys. Rev. Lett.* **120**, 057201 (2018).
26. Y. Iqbal *et al.*, Quantum and classical phases of the pyrochlore Heisenberg model with competing interactions. *Phys. Rev. X* **9**, 011005 (2019).
27. N. Niggemann, Y. Iqbal, J. Reuther, Quantum effects on unconventional pinch point singularities. *Phys. Rev. Lett.* **130**, 196601 (2023).
28. F. Kolley, S. Deppenbrock, I. P. McCulloch, U. Schollwöck, V. Alba, Phase diagram of the  $J_1$ - $J_2$  Heisenberg model on the Kagome lattice. *Phys. Rev. B* **91**, 104418 (2015).
29. M. Pretko, X. Chen, Y. You, Fracton phases of matter. *Int. J. Mod. Phys. A* **35**, 2030003 (2020).
30. S. Onoda, Y. Tanaka, Quantum fluctuations in the effective pseudospin- $\frac{1}{2}$  model for magnetic pyrochlore oxides. *Phys. Rev. B* **83**, 094411 (2011).
31. S. Lee, S. Onoda, L. Balents, Generic quantum spin ice. *Phys. Rev. B* **86**, 104412 (2012).
32. J. G. Rau, M. J. P. Gingras, Frustrated quantum rare-earth pyrochlores. *Annu. Rev. Condens. Matter Phys.* **10**, 357–386 (2019).
33. H. Yan, A. Sanders, C. Castelnovo, A. H. Nevidomskyy, Experimentally tunable QED in dipolar-octupolar quantum spin ice. *arXiv [Preprint]* (2023). <http://arxiv.org/abs/2312.11641> (Accessed 10 May 2024).
34. A. Sanders, C. Castelnovo, Vison crystal in quantum spin ice on the breathing pyrochlore lattice. *Phys. Rev. B* **109**, 094426 (2024).
35. J. Villain, Insulating spin glasses. *Z. Phys. B* **33**, 31 (1979).
36. Y. Katayama *et al.*, A first-order liquid-liquid phase transition in phosphorus. *Nature* **403**, 170 (2000).
37. L. Henry *et al.*, Liquid-liquid transition and critical point in sulfur. *Nature* **584**, 382 (2020).
38. J. N. Hallén, C. Castelnovo, R. Moessner, Thermodynamics and fractal dynamics of a nematic spin ice: A doubly frustrated pyrochlore Ising magnet. *Phys. Rev. B* **109**, 014438 (2024).
39. J. S. Gardner *et al.*, Cooperative paramagnetism in the geometrically frustrated pyrochlore antiferromagnet  $\text{Tb}_2\text{Ti}_2\text{O}_7$ . *Phys. Rev. Lett.* **82**, 1012–1015 (1999).
40. H. Takatsu *et al.*, Order in the frustrated pyrochlore  $\text{Tb}_{2+x}\text{Ti}_{2-x}\text{O}_{7+y}$ . *Phys. Rev. Lett.* **116**, 217201 (2016).
41. H. Yan, O. Benton, L. Jaubert, N. Shannon, Theory of multiple-phase competition in pyrochlore magnets with anisotropic exchange with application to  $\text{Yb}_2\text{Ti}_2\text{O}_7$ ,  $\text{Er}_2\text{Ti}_2\text{O}_7$ , and  $\text{Er}_2\text{Sn}_2\text{O}_7$ . *Phys. Rev. B* **95**, 094422 (2017).
42. V. Noculak *et al.*, Classical and quantum phases of the pyrochlore  $S = \frac{1}{2}$  magnet with Heisenberg and Dzyaloshinskii-Moriya interactions. *Phys. Rev. B* **107**, 214414 (2023).
43. M. Tailleferumier, O. Benton, H. Yan, L. D. C. Jaubert, N. Shannon, Competing spin liquids and hidden spin-nematic order in spin ice with frustrated transverse exchange. *Phys. Rev. X* **7**, 041057 (2017).
44. Y. Kato, S. Onoda, Numerical evidence of quantum melting of spin ice: Quantum-to-classical crossover. *Phys. Rev. Lett.* **115**, 077202 (2015).
45. R. Moessner, J. T. Chalker, Properties of a classical spin liquid: The Heisenberg pyrochlore antiferromagnet. *Phys. Rev. Lett.* **80**, 2929–2932 (1998).
46. R. Moessner, J. T. Chalker, Low-temperature properties of classical geometrically frustrated antiferromagnets. *Phys. Rev. B* **58**, 12049–12062 (1998).
47. C. L. Henley, Effective Hamiltonians and dilution effects in Kagome and related anti-ferromagnets. *Can. J. Phys.* **79**, 1307 (2001).
48. P. H. Conlon, J. T. Chalker, Absent pinch points and emergent clusters: Further neighbor interactions in the pyrochlore Heisenberg antiferromagnet. *Phys. Rev. B* **81**, 224413 (2010).
49. M. Elhadj, B. Canals, R. Sunyer, C. Lacroix, Ordering in the pyrochlore antiferromagnet due to Dzyaloshinsky-Moriya interactions. *Phys. Rev. B* **71**, 094420 (2005).
50. H. Kadowaki, H. Takatsu, T. Taniguchi, B. Fak, J. Ollivier, Composite spin and quadrupole wave in the ordered phase of  $\text{Tb}_{2+x}\text{Ti}_{2-x}\text{O}_{7+y}$ . *SPIN* **5**, 540003 (2015).
51. H. Yan, O. Benton, A. H. Nevidomskyy, R. Moessner, Classification of classical spin liquids: Detailed formalism and suite of examples. *Phys. Rev. B* **109**, 174421 (2024).
52. D. A. Garanin, B. Canals, Classical spin liquid: Exact solution for the infinite-component antiferromagnetic model on the kagomé lattice. *Phys. Rev. B* **59**, 443–456 (1999).
53. S. V. Isakov, K. Gregor, R. Moessner, S. L. Sondhi, Dipolar spin correlations in classical pyrochlore magnets. *Phys. Rev. Lett.* **93**, 167204 (2004).
54. C. L. Henley, Ordering due to disorder in a frustrated vector antiferromagnet. *Phys. Rev. Lett.* **62**, 2056–2059 (1989).
55. A. Prem, S. Vijay, Y. Z. Chou, M. Pretko, R. M. Nandkishore, Pinch point singularities of tensor spin liquids. *Phys. Rev. B* **98**, 165140 (2018).
56. J. T. Chalker, P. C. W. Holdsworth, E. F. Shender, Hidden order in a frustrated system: Properties of the Heisenberg kagomé antiferromagnet. *Phys. Rev. Lett.* **68**, 855–858 (1992).
57. L. R. Walker, R. E. Walsted, Computer model of metallic spin-glasses. *Phys. Rev. B* **22**, 3816–3842 (1980).
58. B. Javanparast, A. G. R. Day, Z. Hao, M. J. P. Gingras, Order-by-disorder near criticality in  $xy$  pyrochlore magnets. *Phys. Rev. B* **91**, 174424 (2015).
59. J. Reuther, P. Wölfle,  $J_1$ - $J_2$  frustrated two-dimensional Heisenberg model: Random phase approximation and functional renormalization group. *Phys. Rev. B* **81**, 144410 (2010).
60. T. Müller *et al.*, Pseudo-fermion functional renormalization group for spin models. *IOP Science* **87**, 036501 (2024).
61. J. Oitmaa, C. Hamer, W. Zheng, *Series Expansion Methods for Strongly Interacting Lattice Models* (Cambridge University Press, 2006).
62. L. Ye, M. E. Sorensen, M. D. Bachmann, I. R. Fisher, Measurement of the magnetic octupole susceptibility of  $\text{PrV}_2\text{Al}_2\text{O}$ . *arXiv [Preprint]* (2023). <https://doi.org/10.48550/arXiv.2309.04633> (Accessed 20 October 2023).
63. A. W. C. Wong, Z. Hao, M. J. P. Gingras, Ground state phase diagram of generic  $xy$  pyrochlore magnets with quantum fluctuations. *Phys. Rev. B* **88**, 144402 (2013).
64. J. D. Alzate-Cardona, D. Sabogal-Suárez, R. F. L. Evans, E. Restrepo-Parra, Optimal phase space sampling for Monte Carlo simulations of Heisenberg spin systems. *J. Phys. Condens. Matter* **31**, 095802 (2019).
65. M. E. Zhitomirsky, M. V. Gvozdkova, P. C. W. Holdsworth, R. Moessner, Quantum order by disorder and accidental soft mode in  $\text{Er}_2\text{Ti}_2\text{O}_7$ . *Phys. Rev. Lett.* **109**, 077204 (2012).
66. M. Creutz, Overrelaxation and Monte Carlo simulation. *Phys. Rev. D* **36**, 515–519 (1987).
67. H. Shinaoka, Y. Tomita, Y. Motome, Loop algorithm for classical antiferromagnetic Heisenberg models with biquadratic interactions. *J. Phys. Conf. Ser.* **320**, 012009 (2011).
68. H. Shinaoka, Y. Motome, Loop algorithm for classical Heisenberg models with spin-ice type degeneracy. *Phys. Rev. B* **82**, 134420 (2010).
69. M. Galassi *et al.*, *GNU Scientific Library Reference Manual* (Network Theory Ltd., ed. 3, 2009).
70. D. Lozano-Gómez *et al.*,  $\text{R1R2\_spin\_liquid\_data}$ . GitHub. [https://github.com/daniel-lozano/R1R2\\_spin\\_liquid\\_data](https://github.com/daniel-lozano/R1R2_spin_liquid_data). Deposited 26 July 2024.